

Broadband Spintronic Terahertz Source with Peak Electric Fields Exceeding 1.5 MV/cm

R. Rouzegar^{1,2,*}, A.L. Chekhov^{1,2,†}, Y. Behovits^{1,2}, B.R. Serrano^{1,2}, M.A. Syskaki^{3,4}, C.H. Lambert⁵, D. Engel⁶, U. Martens⁷, M. Münzenberg⁷, M. Wolf², G. Jakob³, M. Kläui³, T.S. Seifert^{1,2} and T. Kampfrath^{1,2}

¹Department of Physics, Freie Universität Berlin, 14195 Berlin, Germany

²Department of Physical Chemistry, Fritz Haber Institute of the Max Planck Society, 14195 Berlin, Germany


³Institute of Physics, Johannes Gutenberg University Mainz, 55099 Mainz, Germany

⁴Singulus Technologies, 63796 Kahl am Main, Germany

⁵Department of Materials, ETH Zürich, CH-8093 Zürich, Switzerland

⁶Max-Born-Institut für nichtlineare Optik und Kurzzeitspektroskopie, 12489 Berlin, Germany

⁷Institut für Physik, Universität Greifswald, 17489 Greifswald, Germany

 (Received 7 November 2022; revised 23 December 2022; accepted 24 January 2023; published 6 March 2023)

In this work, we improve the performance of an optically pumped spintronic terahertz emitter (STE) by a factor of up to 6 in field amplitude through an optimized photonic and thermal environment. Using high-energy pump pulses (energy 5 mJ, fluence >1 mJ/cm², wavelength 800 nm, duration 80 fs), we routinely generate terahertz pulses with focal peak electric fields above 1.5 MV/cm, fluences of the order of 1 mJ/cm², and a spectrum covering the range 0.1–11 THz. Remarkably, the field and fluence values are comparable to those obtained from a state-of-the-art terahertz table-top high-field source based on tilted-pulse-front optical rectification in LiNbO₃. The optimized STE inherits all attractive features of the standard STE design, for example, ease of use and the straightforward rotation of the terahertz polarization plane, without the typical 75% power loss found in LiNbO₃ setups. It, thus, opens up a promising pathway to nonlinear terahertz spectroscopy. Using low-energy laser pulses (2 nJ, 0.2 mJ/cm², 800 nm, 10 fs), the emitted terahertz pulse has a focal peak electric field of 100 V/cm, which corresponds to a 2-fold improvement, and covers the spectrum 0.3–30 THz.

DOI: [10.1103/PhysRevApplied.19.034018](https://doi.org/10.1103/PhysRevApplied.19.034018)

I. INTRODUCTION

Terahertz radiation, which covers the range 0.1–30 THz, is a powerful tool to spectroscopically study fundamental modes of matter, for example, electronic intraband transport, magnons, or phonons in solids [1,2]. Thus, efficient broadband terahertz sources are of large interest for linear spectroscopy to extract the linear optical response over a large spectral range or the thickness of a known material with high precision [3]. On the other hand, high-amplitude terahertz sources are important, too, because they enable one to not only probe but also drive numerous elementary

excitations. This approach allows one to disentangle fundamental interactions between different subsystems or to push various degrees of freedom into highly nonlinear regimes [4–7].

Laser-driven table-top terahertz emitters are typically based on (1) resonantly induced photocurrents or (2) off-resonant charge motion, also termed optical rectification. Examples of (1) include photoconductive antennas [8–10], shift-current emitters [11], laser-ionized gases [12–15], and spintronic terahertz emitters (STEs) [16–21]. Examples of (2) are inorganic crystals, such as ZnTe, GaP, and LiNbO₃ [19,22,23], and organic materials like N-benzyl-2-methyl-4-nitroaniline (BNA) [24–27].

Photoconductive antennas are commonly used sources for linear terahertz spectroscopy, and they can generate terahertz pulses with peak fields up to 200 kV/cm at kilohertz repetition rates with a spectral bandwidth that is typically limited to <6 THz at 10% of the amplitude maximum [8,9]. More broadband terahertz pulses with fields up to 1 kV/cm at megahertz rates can be generated by ultrafast shift currents upon resonant interband photoexcitation of

*m.rouzegar@fu-berlin.de

†These authors contributed equally.

Published by the American Physical Society under the terms of the Creative Commons Attribution 4.0 International license. Further distribution of this work must maintain attribution to the author(s) and the published article's title, journal citation, and DOI. Open access publication funded by the Max Planck Society.

quantum-well emitters [11]. Organic crystals cover different terahertz frequency ranges at large field strengths of more than 2 MV/cm [24]. They are typically affected by gaps in the 1–10 THz window [25–27] and often require infrared wavelengths for pumping and, thus, optical parametric amplifiers for prior frequency conversion. Their long-term stability can be impacted by the applied pump laser fluence and power [28]. Air-plasma terahertz sources offer gapless terahertz radiation over the range 1–40 THz [13] with the peak electric field reaching 0.4 MV/cm [14]. However, they require pump pulses with energies above around 0.1 mJ and react sensitively to laser and setup fluctuations [20,29].

In terms of high-field terahertz sources, LiNbO₃ is a workhorse of nonlinear terahertz spectroscopy and delivers peak fields beyond 1 MV/cm with a spectrum of 0.1–3.5 THz [22,23,30–32]. Rotation of the terahertz polarization plane often relies on projection operations by 2 wire-grid polarizers and is accompanied by an amplitude reduction of up to 50%. The terahertz-source alignment is challenging because it requires a tilted-pulse-front scheme for phase matching and a reflective telescope for tight terahertz-beam focusing [31].

Spintronic terahertz emitters (STEs) offer significant potential as terahertz sources, since they combine many benefits of other emitter types [16,20,21,33–48]. In particular, STEs permit generation of broadband and single-cycle terahertz pulses independent of the pump wavelength and pump polarization. The alignment is straightforward, and control of the terahertz polarization or even polarization landscape is easy using an external magnetic field [49–52]. Although the approach is easily scalable with regard to the STE area and, thus, pump-pulse energy, peak fields are, so far, limited to 0.3 MV/cm [17]. However, to drive nonlinear processes and achieve sufficient signal strengths, peak terahertz fields exceeding 1 MV/cm and fluences of the order of 1 mJ/cm² are highly desirable.

In this work, we improve the performance of a STE by optimizing the management of light and heat flow. Our photonic and thermal modifications allow us to generate terahertz pulses with peak electric fields above 1.5 MV/cm and fluences above 1 mJ/cm² for 800 nm, 5 mJ pump pulses. The covered spectral range 0.1–11 THz is limited primarily by the pump-pulse duration. Remarkably, the field and fluence values are comparable to those obtained from a state-of-the-art terahertz table-top high-field source based on LiNbO₃. The optimized STE still has all the attractive features of the standard STE, for instance, the straightforward rotation of the terahertz polarization plane, which is important for nonlinear spectroscopic applications. In particular, the terahertz field can be reversed easily without the typical 75% power loss found in LiNbO₃ setups. We demonstrate the power of the optimized STE in terahertz-pump optical-probe experiments.

A. Standard STE design

The conventional STE design is shown in Fig. 1(a). It is based on a substrate, such as glass or sapphire, on top of which a spintronic trilayer stack W(2 nm)|Co₂₀Fe₆₀B₂₀(1.8 nm)|Pt(2 nm) is grown [Fig. 1(b)]. The magnetization \mathbf{M} of the ferromagnetic Co₂₀Fe₆₀B₂₀ (CFB) layer is set by an external magnetic field. An incident femtosecond laser pulse deposits excess energy in the electrons of CFB, resulting in a transient generalized spin voltage that drives a spin current from CFB into the Pt and W layers [53–56]. The inverse spin Hall effect (ISHE) of Pt and W converts the spin current into an ultrafast in-plane charge current that emits an electromagnetic pulse with frequencies extending into the terahertz range. The terahertz waves from Pt and W add constructively because Pt and W have spin Hall angles of opposite sign [16,57].

Building on its success [16,17,20,58–62], the STE design of Fig. 1(a) can be improved further. First, the transfer of excess energy into the substrate by heat flow is suboptimal for glass substrates used previously [17,63]. The energy deposited by the pump beam can lead to a stationary increase of the working temperature of the STE. As a consequence, each single pump pulse will more easily increase the transient electronic temperature above the Curie temperature of the magnetic layer, resulting in saturation of the STE terahertz output versus pump power [18].

Second, only 50%–60% of the incident pump power is absorbed in the trilayer. This value can be increased to >90% by using dielectric cavities [63,64]. The residual transmitted pump can cause disturbance and is, thus, usually removed by subsequent filtering [17].

Finally, the terahertz-pulse outcoupling into the forward direction is not ideal because about 75% of the generated terahertz electromagnetic power is emitted into the backward direction, i.e., into the substrate. To illustrate this behavior, we calculate the terahertz electric-field amplitude by a transfer-matrix approach [65], the result of which is shown by the red solid line in Fig. 1(a).

B. Si-based STE design

To address the three challenges identified above, we introduce a Si-based STE [Si-STE, see Fig. 1(c)], which has an optimized photonic and thermal environment. First, to minimize the steady-state temperature increase of the metal films due to excess energy accumulation, substrates with good thermal conductivity at 300 K are required. Therefore, Si (150 W/m K), diamond (1500 W/m K), and sapphire (30 W/m K) are very good candidate materials [66–68], but glass (1.5 W/m K) is not [69]. As shown in the following, Si is the most suitable choice.

Second, to optimize the photonic environment, we note that the terahertz electric field leaving the STE increases

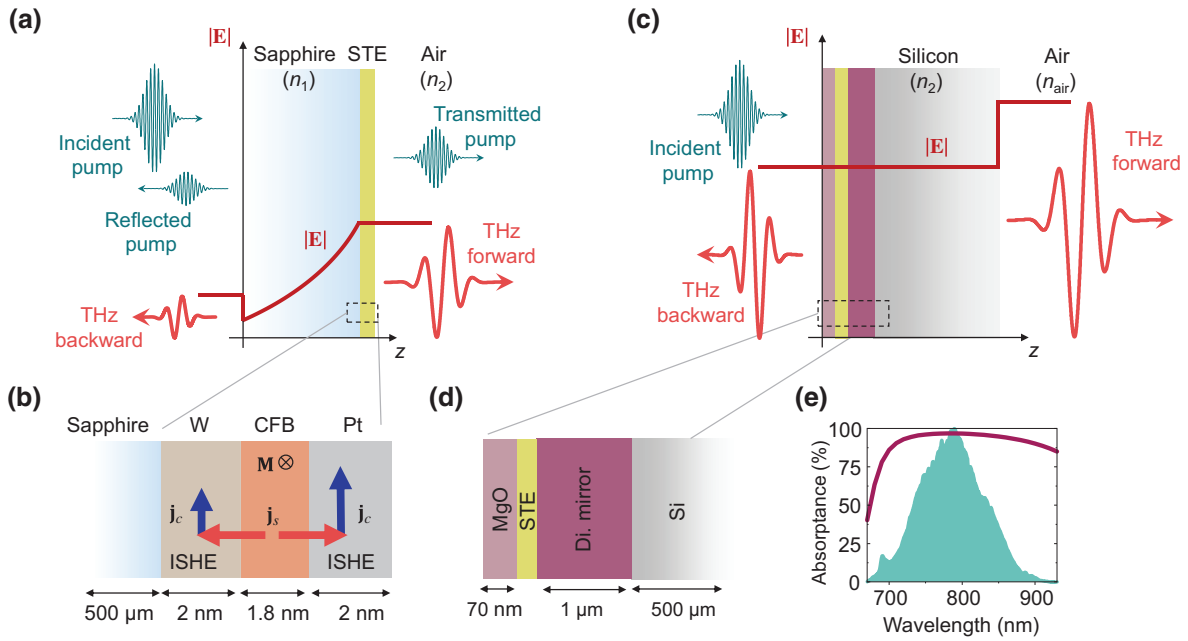


FIG. 1. Two photonic and thermal environments of the STE. (a) Standard STE configuration. An incident pump pulse (teal) deposits 50%–60% of its energy in a metallic STE stack (yellow), resulting in the emission of a terahertz electromagnetic pulse (red). The red solid line indicates the calculated terahertz electric-field amplitude. The backward-propagating terahertz field is strongly attenuated in the sapphire substrate but increases abruptly when traversing the interface to air. (b) The STE stack is a metallic trilayer, W(2 nm)|CFB(1.8 nm)|Pt(2 nm), in which the ferromagnetic CFB layer has in-plane magnetization \mathbf{M} . Pump excitation induces a spin voltage that injects a spin current \mathbf{j}_s into the adjacent Pt and W paramagnetic layers. In these layers, the ISHE transforms \mathbf{j}_s into a transverse charge current \mathbf{j}_c that acts as a source of a terahertz electromagnetic pulse propagating forward and backward. (c) Si-based STE (Si-STE) design with a >2 times larger forward-propagating electric field. The enhancement relies on $>95\%$ deposition of the pump pulse in the STE stack, negligible attenuation in the Si, and the discontinuity of the forward-propagating terahertz electric field at the Si/air interface. (d) Si-STE design details. The STE is sandwiched between a dielectric mirror [$\text{SiO}_2(165 \text{ nm})|\text{TiO}_2(94 \text{ nm})_5$] and a MgO layer, which minimize pump transmission into Si and reflection into air. (e) Calculated fraction A_p of the incident pump energy that is absorbed in the STE metal stack (purple curve) and measured pump-pulse intensity spectrum of the low-energy setup (green).

monotonically with the pump absorptance A_p of the spintronic trilayer and the impedance of the STE, including any substrates, capping, and buffer layers. The figure of merit Φ for the forward-propagating terahertz wave, which is the direction of interest, can, thus, be written as

$$\Phi = \left| \frac{Z_0}{n_1 + n_2 + Z_0/R_{\text{sh}}} e^{i\omega n_2 d_2/c} \frac{2n_2}{n_2 + n_{\text{air}}} \right| A_p. \quad (1)$$

The first factor on the right-hand side of Eq. (1) is the impedance of the STE alone, i.e., as sandwiched between half-spaces with terahertz refractive indices n_1 and n_2 [16]. The second factor accounts for the terahertz-pulse propagation through the window (refractive index n_2 and finite thickness d_2) behind the STE, while the third factor is a Fresnel coefficient that quantifies the transmission into air (refractive index $n_{\text{air}} \approx 1$). Here, $Z_0 \approx 377 \Omega$ and c are, respectively, the impedance and light velocity of free space, and $R_{\text{sh}} \approx 140 \Omega$ is the sheet resistance of the STE

metal trilayer measured with a 4-point probe. The last factor, A_p , is the fraction of the incident pump-pulse energy that is absorbed in the STE metal stack.

In the previous STE design [see Fig. 1(a)] [16,17,63], the first window is the glass or sapphire substrate of the trilayer, and the second window is air ($n_2 = n_{\text{air}}$, $d_2 = 0$). The resulting evolution of the terahertz field amplitude [red solid line in Fig. 1(a)] shows that the backward-traveling wave is strongly attenuated by the sapphire window (see Fig. S1 [70]). Because the refractive index of sapphire exhibits sharp spectral features and shows up in the impedance [first factor in Eq. (1)], the spectrum of the forward-emitted wave is also frequency dependent [59]. At a wavelength of 800 nm, the pump absorptance is $A_p = 0.6$, as indicated by the reflected and transmitted pump pulses in Fig. 1(a).

To enhance the forward-emitted terahertz amplitude, we propose the Si-STE design of Fig. 1(c), which relies on the idea that most of the terahertz electromagnetic energy generated in the trilayer propagates into the adjacent window with the larger refractive index (see Fig. S2

[70]). Consequently, we choose air ($n_1 \approx 1$) as the first half-space and high-resistivity Si ($n_2 \approx 3.4 \gg n_1$) as the second. These 2 media exhibit a spectrally flat refractive index with negligible attenuation throughout the range 0.3–30 THz. Diamond has similarly promising terahertz-optical properties as Si, but is not considered further because of its high cost for upscaling to 5-cm size. Sapphire is discarded, too, because of its significant terahertz-wave attenuation [see Fig. 1(a) and Fig. S1 [70]].

Note that the Si-STE configuration air|Pt|CFB|W|Si increases the product of the first three factors in Eq. (1) by 44% compared to the previous STE design based on glass or sapphire substrates [Fig. 1(a)]. The major reason is the increased transmission from Si (n_2) to air (third factor), which amounts to 1.55. It still overcompensates for the decreased trilayer impedance (first factor), which equals 57Ω and 53Ω in the standard STE and Si-STE designs, respectively. This effect is confirmed by the calculated spatial evolution of the terahertz field amplitude [red line in Fig. 1(c)], which exhibits a significant amplitude increase at the Si/air interface.

Third and finally, we embed the trilayer between a dielectric mirror [$\text{SiO}_2(165 \text{ nm})|\text{TiO}_2(94 \text{ nm})_5$] and an impedance-matching layer MgO(70 nm) [see Fig. 1(d)] [63]. In this way, we push the pump absorptance from $A_p = 60\%$ in the sapphire-based STE [Fig. 1(a)] to a calculated value $>95\%$ in the Si-STE in the range 740–840 nm [Fig. 1(e)]. The pump reflectance is reduced to $<3\%$, as indicated by the absence of reflected and transmitted pump pulses in Fig. 1(c). The dielectric mirror also reduces the amount of pump-induced free charge carriers in Si to $<1\%$, which may otherwise attenuate and distort the terahertz pulse.

The terahertz amplitude evolution [red solid lines in Figs. 1(a) and 1(c)] summarizes the benefits of the optimized STE [Fig. 1(c)] relative to the previous design [Fig. 1(a)]. In the standard STE, around 25% of the emitted terahertz power propagates into the far field in the forward direction, whereas it is about 55% in the Si-STE design.

II. EXPERIMENTAL DETAILS

A. STE fabrication and characterization

STE trilayers W(2 nm)| $\text{Co}_{20}\text{Fe}_{60}\text{B}_{20}$ (1.8 nm)|Pt(2 nm) are deposited on top of Si|dielectric mirror or sapphire substrates using a Singulus Rotaris magnetron tool with a base pressure of 4×10^{-8} mbar by dc-magnetron sputtering. Radio-frequency sputtering is used for the MgO(70 nm) impedance-matching layer from a composite MgO target. The deposition rates for Pt, W, CFB, and MgO are 0.91, 1.58, 0.66, and 0.09 \AA s^{-1} , respectively, under the pure Ar flow used as the sputtering gas. The double-side-polished Si wafer has a resistivity $>10 \text{ k}\Omega/\text{cm}$. The dielectric mirror [$\text{SiO}_2(165 \text{ nm})|\text{TiO}_2(94 \text{ nm})_5$] is grown on top of the Si (Siegert Wafer GmbH).

For STEs with pump-transparent substrate, such as sapphire [Fig. 1(a)], the pump absorptance A_p of the STE metal stack is experimentally determined by measuring the fractions of the reflected (R) and transmitted (T) pump power through $A_p = 1 - R - T$.

For the Si-STE, we find zero reflectance and transmittance into air within the accuracy of our measurement of around 1%. Therefore, 100% of the pump power is absorbed in the Si-STE metal stack and the Si substrate. To estimate the pump power entering the Si substrate, we separately measure the reflectance of the dielectric-mirror stack on top of the Si slab and find it to be $>95\%$. We, thus, expect a pump transmittance $T < 5\%$ into the Si substrate for the Si-STE, resulting in $A_p = 1 - R - T > 95\%$. This result is consistent with our calculations in the range of the pump-pulse spectrum [Fig. 1(e)].

B. Low- and high-energy terahertz setups

To put our expectations to test, standard STEs and Si-STE (TeraSpinTec GmbH) are excited with femtosecond laser pulses, and their terahertz emission is measured in a low-energy (pulse energy 2 nJ, fluence $0.2 \text{ mJ}/\text{cm}^2$) and high-energy (5 mJ, $1 \text{ mJ}/\text{cm}^2$) regime. The dielectric layers and the STE trilayers are grown by sputter deposition on Si or sapphire substrates.

In the experiment, a homogeneous distribution of the in-plane magnetization \mathbf{M} of the STE's CFB layer is achieved by an external magnetic field of approximately 10 mT, which is provided by a Halbach array of permanent magnets [71] (see Fig. S3 [70]). As the array is rigidly connected to the STE, rotation of the STE allows us to rotate the CFB magnetization \mathbf{M} in the plane.

For low-energy operation [Fig. 2(a)], laser pulses [bandwidth-limited duration about 10 fs full width at half maximum (FWHM) of intensity, center wavelength 800 nm, repetition rate 80 MHz, pulse energy up to 2 nJ, intensity spectrum in Fig. 1(e)] are focused onto the STE surface with a spot size of 30 μm , resulting in a maximum incident fluence of $0.2 \text{ mJ}/\text{cm}^2$. By using 2 90° -off-axis parabolic mirrors, the generated terahertz pulse is focused into a ZnTe(110) crystal (thickness 10 μm) glued to a ZnTe(100) substrate [72], where its electric field is monitored by electro-optic sampling (EOS) with laser pulses from the same laser.

The resulting signal $S(t)$ with time t and the terahertz electric field $\mathbf{E}(t)$ incident onto the detection crystal are in the frequency domain connected by [72,73]

$$\tilde{S}(\omega) = \tilde{H}_{\text{EOS}}(\omega)\tilde{E}(\omega). \quad (2)$$

Here, the tilde denotes Fourier transformation, $\omega/2\pi$ is frequency, and $\tilde{H}_{\text{EOS}}(\omega)$ is the transfer function of the EOS process. We note that EOS acts akin to a polarizer that projects the terahertz electric-field vector \mathbf{E} onto a

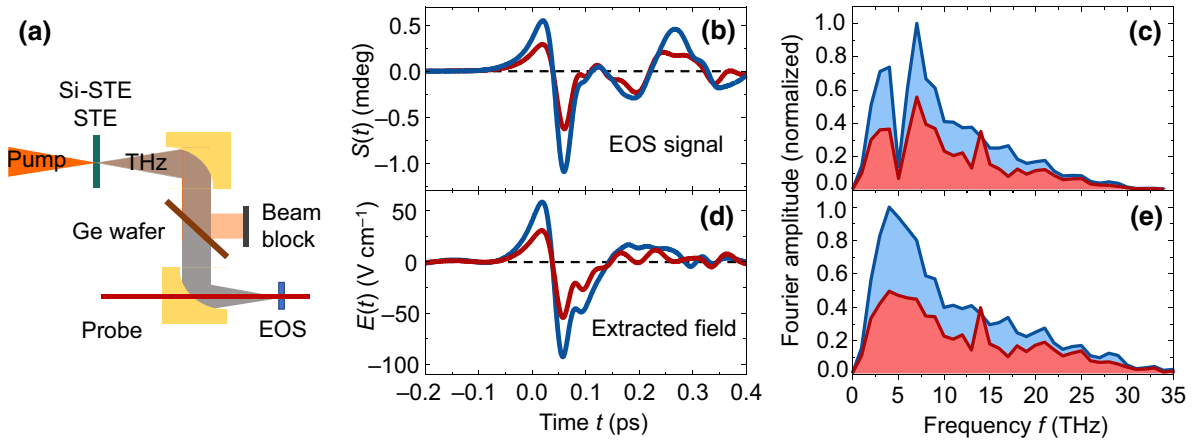


FIG. 2. Low-energy STE operation. (a) Schematic of the setup. A laser pulse [bandwidth-limited duration 10 fs, spectrum in Fig. 1(e)] is focused into the STE (incident fluence 0.2 mJ/cm^2). The resulting terahertz pulse is collimated with a parabolic mirror and focused into a ZnTe(110) crystal (thickness $10 \mu\text{m}$) for EOS by the probe pulse. (b) Terahertz electro-optic signal waveforms (probe ellipticity) obtained from a standard STE and a Si-STE [Figs. 1(a) and 1(c)]. (c) Fourier amplitude of the terahertz signals shown in panel (b). (d) Extracted electric field from the signals shown in panel (b). (e) Fourier amplitude of the extracted electric field.

direction \mathbf{v} with $|\mathbf{v}| = 1$. Therefore,

$$E(t) = \mathbf{v} \cdot \mathbf{E}(t), \quad (3)$$

where \mathbf{v} is given by the azimuthal angle of the ZnTe crystal and the direction of the probe polarization [74].

For high-energy operation [Figs. 3(a) and 3(b)], pump pulses (35 fs if bandwidth-limited, 800 nm, 1 kHz, up to 5 mJ) are derived from an amplified Ti:sapphire laser system. The collimated pump beam is enlarged to a width of 2 cm (FWHM of intensity) using a telescope, resulting in an incident fluence of up to 1.1 mJ/cm^2 . The generated terahertz beam is focused into a ZnTe(110) crystal (thickness $10 \mu\text{m}$) for electro-optic sampling using pulses (20 fs if bandwidth-limited, 800 nm, 80 MHz, $<1 \text{ nJ}$) from the seed laser oscillator [75,76]. The terahertz power is measured by a power meter (GenTec THZ9B-BL-DZ-D0). The approximate intensity distribution of the beam cross section in the terahertz focus is obtained by placing a microbolometer array (Xenics Gobi + 640) at the position of the electro-optic crystal [Fig. 3(c)].

In both setups, the standard STE is pumped from the substrate side. The pump radiation traversing the STE is filtered out by a Ge wafer (low-power setup) or a combination of an ITO dichroic mirror and a Si window at the Brewster angle (high-power setup). In contrast, the Si-STE is excited from the air side. As no pump radiation traverses the Si-STE, no further filtering of the beam is required.

Finally, as a reference of the STE under high-fluence operation, we employ a state-of-the-art terahertz source based on tilted-pulse-front excitation of a LiNbO₃ prism. It is driven by pump pulses analogous to the STE, but time-stretched and with slightly less energy (400 fs, 4.2 mJ) to avoid crystal damage [7,19,22,77].

III. RESULTS

A. Low-energy megahertz operation

Figure 2(b) shows terahertz signal waveforms $S(t)$ from a standard STE and a Si-STE. We find that the Si-STE delivers an amplitude that is a factor of 2 larger than that from the standard STE. This value reaches almost the ideal enhancement factor of 2.3 [see Figs. 1(a) and 1(c)]. We ascribe the minor discrepancy to the astigmatism that arises as the strongly divergent terahertz beam traverses the Si window of the Si-STE (see Fig. S2 [70]).

The amplitude spectrum $|\hat{S}(\omega)|$ of the terahertz signal is shown in Fig. 2(c). The dip at frequency $\omega/2\pi \approx 5 \text{ THz}$ arises from a zero of the EOS transfer function $\hat{H}_{\text{EOS}}(\omega)$ of the ZnTe crystal [Eq. (2)] [72] and results in temporal oscillations of $S(t)$, as seen in Fig. 2(a) and Fig. S4 [70].

To extract the transient terahertz electric field $E(t)$ in the beam focus right in front of the electro-optic detection crystal, we make use of Eq. (2) and deconvolute the calculated $\hat{H}_{\text{EOS}}(\omega)$ [73] from the measured terahertz signal waveform [78–80] (see Fig. S4 [70]). The resulting field $E(t)$ is shown in Fig. 2(d). We find a peak field of approximately 100 V/cm .

For both emitters, the spectrum of the electric field covers the range 0.3–30 THz at the 10% level of the peak amplitude [Fig. 2(e)]. The Si-STE spectrum is smoother compared with the standard STE since the frequency dependence of the Si refractive index is substantially smoother than that of sapphire, in particular in the range 12–14 THz [59].

To summarize, under low-energy operation, the Si-STE design provides a factor of 2 higher amplitude of the emitted terahertz field compared with the standard STE. This increase is only slightly smaller than our expectation of

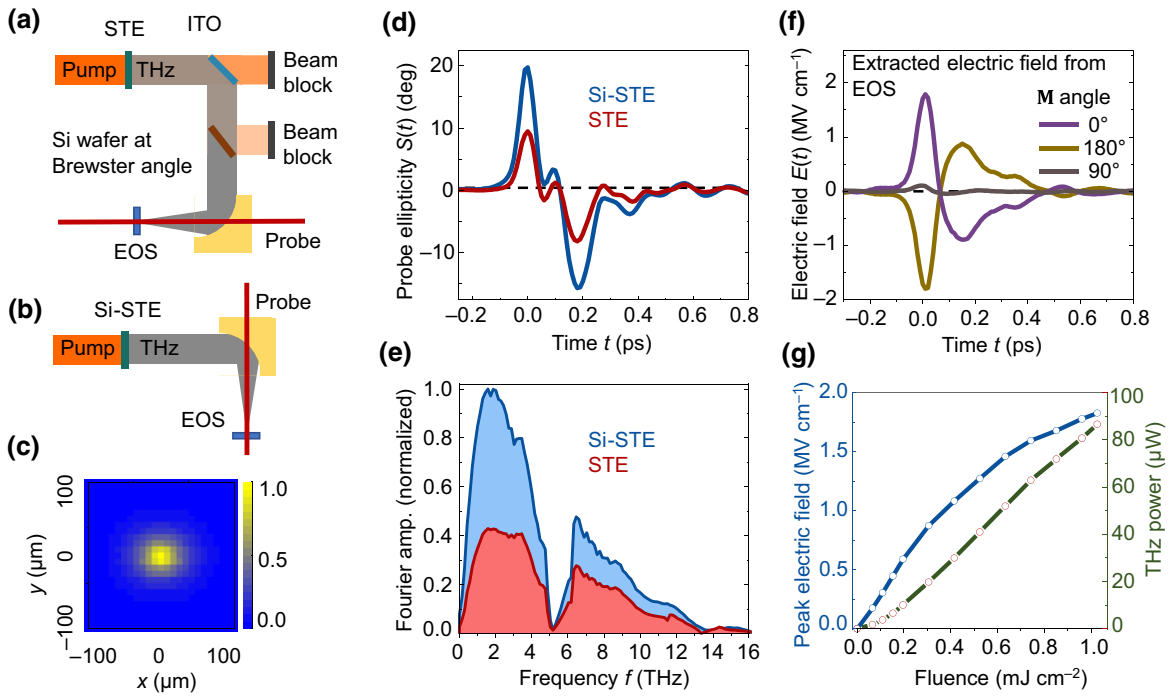


FIG. 3. High-energy STE operation. (a),(b) Schematics of the setups. (a) The collimated pump-pulse beam (35 fs if bandwidth-limited, 800 nm, 5 mJ, 1.1 mJ/cm^2) is partially transmitted by the STE on sapphire and removed by an ITO dichroic mirror and Si wafer. (b) In contrast, the Si-STE fully absorbs the pump beam. The generated terahertz beam is focused into a ZnTe(110) crystal (thickness $10 \mu\text{m}$) for EOS by the probe pulse. (c) Intensity distribution of the Si-STE terahertz-beam focus as measured with a microbolometer array. (d) Electro-optic signal of STE and Si-STE terahertz pulses and (e) their amplitude spectra. (f) Focal terahertz electric field of Si-STE extracted from the electro-optic signals for three magnetization directions of the Si-STE. The detector is insensitive to the terahertz electric field emitted at 90° magnetization orientation. (g) Measured terahertz power and peak electric field versus incident and, thus, absorbed pump fluence for the Si-STE.

the 1.4-fold higher terahertz outcoupling and the 1.6-fold higher pump absorptance. According to the photocurrent generation mechanism of the STE, the amplitude fluctuations of the terahertz pulses scale with the energy fluctuations of the pump pulses and, thus, the stability of the pump laser. The fluctuations of the measured terahertz signal waveforms depend, in addition, on the stability of the whole terahertz time-domain spectrometer (see Fig. S5 [70]).

B. High-energy kilohertz operation

Figure 3(c) shows the spatially resolved intensity of the focused terahertz beam from the large-area Si-STE as measured by the microbolometer array. The terahertz spot has a circular shape and a width of about $100 \mu\text{m}$ (FWHM of the intensity). At the highest excitation fluence (1.1 mJ/cm^2), we measure a terahertz pulse energy of 90 nJ. Remarkably, this value is more than 1 order of magnitude larger than reported previously using a large-area STE design on a glass substrate [17].

Electro-optic signal waveforms $S(t)$ of the emitted terahertz pulses and their amplitude spectra $|\tilde{S}(\omega)|$ are shown in Figs. 3(d) and 3(e). As in the low-energy case,

the Si-STE is found to outperform the standard STE on sapphire and provides even a factor >2 larger terahertz signal strength. At the same time, the temporal [Fig. 3(d)] and spectral [Fig. 3(e)] shapes of the two STE designs remain approximately the same.

The extracted electric field $E(t)$ in the beam focus is shown in Fig. 3(f). We find a peak electric field of $1.7 \pm 0.2 \text{ MV/cm}$, which implies a peak magnetic field of $0.6 \pm 0.1 \text{ T}$. Time integration over $E^2(t)/Z_0$ yields an incident fluence of $0.7 \pm 0.1 \text{ mJ/cm}^2$ in the beam center. This value is fully consistent with the measured spot size ($100 \mu\text{m}$) and energy (90 nJ) of the terahertz pulse, which imply a fluence of 0.8 mJ/cm^2 [70]. Note that both the microbolometer array and the power meter most likely have a frequency-dependent response over the large STE bandwidth, implying some uncertainty of the measured terahertz power and spot size.

The terahertz field can be perfectly reversed by a 180° rotation of the emitter. If we rotate the emitter by 90° , the extracted field approaches zero [Fig. 3(f)]. As the electro-optic detector is polarization-sensitive [Eq. (3)], this finding indicates that the emitted terahertz pulse is indeed linearly polarized. The polarization direction can be directly controlled by the emitter rotation. Power measurements

confirm that the emitted terahertz power is independent of the polarization of the emitted terahertz radiation (see Fig. S3 [70]).

The terahertz peak field and pulse energy as a function of the incident and, thus, absorbed pump fluence are shown by Fig. 3(g). The fluence scaling of the terahertz pulse energy changes from quadratic to linear at a fluence of around 0.2 mJ/cm². Note that this value is more than a factor of 3 larger than in previous work in which a glass substrate was used [17], as expected from the significantly higher heat conductivity of the Si-STE's Si substrate. Therefore, to operate the Si-STE in the field-linear-with-fluence regime, the pump fluence should be kept at about 0.2 mJ/cm² or below. Interestingly, in this mode, the terahertz field in the center of the terahertz beam focus is independent of the pump-beam diameter because an increased pump diameter implies a smaller terahertz focus size that compensates for the decreased fluence [17,62].

We summarize that, under high-energy operation, the Si-STE design provides a factor of 2.1 larger amplitude of the emitted terahertz field compared with the standard STE on sapphire. This performance improvement agrees well with our results from low-energy operation. It follows our expectations of a 1.4-fold higher terahertz outcoupling and a (1.6)^{0.5}-fold higher pump absorptance, where the exponent 0.5 arises from the fluence dependence [Fig. 3(g)]. The remaining amplitude enhancement of 1.2 is ascribed to the higher heat conductivity of Si as compared with sapphire. The 6-fold amplitude enhancement relative to the previously demonstrated glass-based large-area STE [17] is even more dramatic. We primarily assign it to the much higher heat conductivity of Si relative to glass.

C. Terahertz waveform shape

To understand the shape of the terahertz electric-field waveform $E(t)$ [Figs. 3(f) and 4], we note that the instantaneous terahertz electric field behind the STE metal stack is proportional to the instantaneous sheet charge current $I_c(t)$ in the STE [16,57]. The latter can be described by the convolution [53]

$$I_c(t) \propto (H_{\text{STE}} * \mathbf{E}_p^2)(t) \quad (4)$$

of the squared pump electric field $\mathbf{E}_p^2(t)$ and the STE response function

$$H_{\text{STE}}(t) = \Theta(t)(A_{\text{es}}e^{-\Gamma_{\text{es}}t} - A_{\text{ep}}e^{-\Gamma_{\text{ep}}t}). \quad (5)$$

Here, $\Theta(t)$ is the Heaviside step function, $A_{\text{es}} = (\Gamma_{\text{es}} - r\Gamma_{\text{ep}})/(\Gamma_{\text{es}} - \Gamma_{\text{ep}})$, $A_{\text{ep}} = (1 - r)\Gamma_{\text{ep}}/(\Gamma_{\text{es}} - \Gamma_{\text{ep}})$, Γ_{es}^{-1} and Γ_{ep}^{-1} are material-dependent time constants of electron-spin and electron-phonon relaxation, and r is the ratio of electronic and total heat capacity of the metal stack. The terahertz field $E(t)$ in the focus is approximately proportional

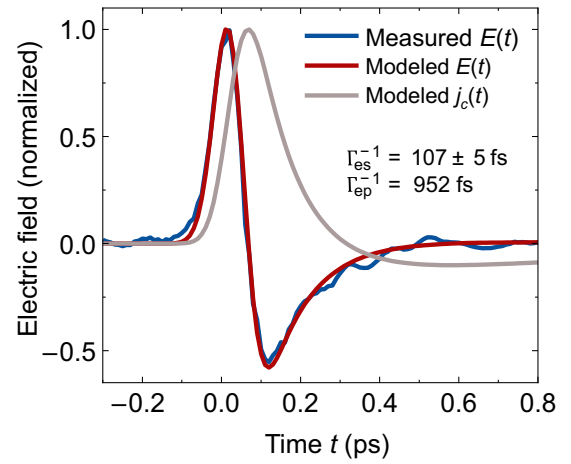


FIG. 4. Measured and modeled dynamics of the focal electric field from the Si-STE. The blue curve shows the electric field $E(t)$ extracted from the electro-optical signal $S(t)$. The red curve is a fit according to Eqs. (4) and (6) with $\Gamma_{\text{es}}^{-1} = 107 \pm 5$ fs and the pump-pulse duration of 84 fs (FWHM intensity) as fit parameters. The gray curve shows the resulting charge current inside the Si-STE metal stack.

to the time-derivative of $I_c(t)$ [17], i.e.,

$$E(t) \propto \partial_t I_c(t). \quad (6)$$

We calculate Γ_{ep} and r according to Ref. [53] and obtain $\Gamma_{\text{ep}}^{-1} = 950$ fs and $r = 0.15$ for the fluence of 1 mJ/cm² used in our experiment. We fit the extracted terahertz field $E(t)$ by Eqs. (4) and (6), where Γ_{es} and the duration of the Gaussian pump intensity profile $\mathbf{E}_p^2(t)$ are fit parameters.

An excellent fit is obtained for $\Gamma_{\text{es}}^{-1} = 107 \pm 5$ fs and a pump-pulse duration of 84 ± 3 fs (FWHM of the intensity) as shown in Fig. 4. The pump duration is a factor >2 longer than that of a bandwidth-limited pump pulse (35 fs) and likely arises from chromatic dispersion of the telescope lenses before the STE, which cannot be compensated for entirely.

To summarize, in the dynamics $E(t)$ of the focal electric field of Fig. 4, the width of the first (positive) peak and of the leading edge of the second (negative) peak is predominantly determined by the pump-pulse duration. The width of the relaxation tail of the second peak is given by both the pump duration and the electron-spin relaxation time Γ_{es}^{-1} of the STE.

D. Comparison with LiNbO3 source

To evaluate the Si-STE performance, we compare it with the gold standard of laser-driven table-top high-power terahertz sources: a state-of-the-art LiNbO₃ source. Figure 5(a) shows the transient terahertz electric field generated by the Si-STE and the LiNbO₃ source. We find similar terahertz peak fields above 1 MV/cm for LiNbO₃ [22,81] and 1.5 MV/cm for the Si-STE.

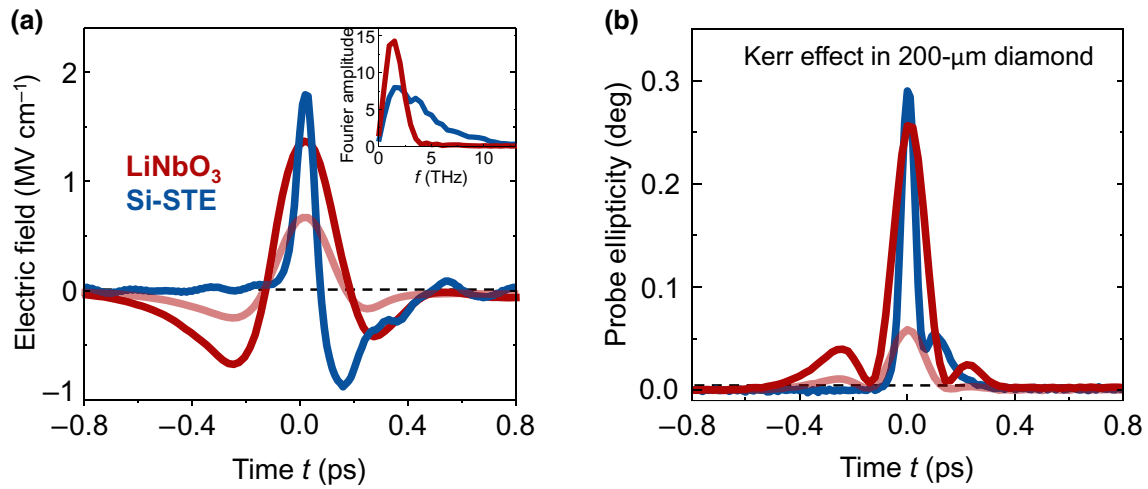


FIG. 5. Quantitative back-to-back comparison of nonlinear terahertz spectroscopy with terahertz pulses from an Si-STE (blue solid lines) versus a LiNbO₃ source without (red solid lines) and with polarizers (light-red solid lines) enabling terahertz field reversal from $\mathbf{E}(t)$ to $-\mathbf{E}(t)$. (a) Electric fields obtained with a ZnTe(110) detector (thickness 10 μm). The inset shows the Fourier amplitude of the electric fields. (b) Signal of terahertz Kerr effect $\propto E^2$ in a diamond window (thickness 200 μm). The resulting optical birefringence is probed by a pulse polarized at 45° with respect to the direction of \mathbf{E} .

However, the two sources are complementary in terms of spectral content as they cover the different spectral ranges 0.1–3.5 THz (LiNbO₃) and 0.1–11 THz (Si-STE) at the 10% amplitude level. Accordingly, the pulses have durations of 500 fs (LiNbO₃) and 200 fs (Si-STE) FWHM of the field envelope (see Fig. S6 [70]). The terahertz fluences are comparable, too, and amount to 1.1 mJ/cm² (LiNbO₃) and 0.7 mJ/cm² (Si-STE).

As a further check, we use the terahertz pulses from the Si-STE and LiNbO₃ sources as pump pulses to induce a transient birefringence that scales quadratically rather than linearly with the instantaneous off-resonant terahertz pump field: the terahertz Kerr effect in a diamond window (thickness 200 μm) [77,82]. The probe is polarized at 45° relative to the terahertz field, and we measure the induced linear birefringence by the ellipticity the optical probe acquires upon propagation through the sample.

Typical signals are displayed in Fig. 5(b). As expected, they are unipolar and approximately proportional to the squared terahertz electric fields [Fig. 5(a)], resulting in substantially faster dynamics for the Si-STE than the LiNbO₃ pulse. Deviations from the instantaneous scaling $\propto E^2(t)$ are ascribed to a mismatch of the propagation velocities of pump and probe pulses (see Fig. S7 [70]) and, possibly, a noninstantaneous terahertz Kerr effect of diamond [83]. Consistent with Fig. 5(a), the responses are of similar amplitude.

We emphasize that, in a substantial number of nonlinear terahertz experiments, odd and even signal contributions in the driving terahertz field occur. To separate them, one needs to measure the sample response to both the terahertz field $\mathbf{E}(t)$ and its reversed version $-\mathbf{E}(t)$. Examples

are studies in ultrafast magnetism [75,84] and terahertz scanning tunneling microscopy [85,86].

The terahertz electric field from the Si-STE can be reversed without loss in terahertz power by rotating the external magnetic field by 180° . In contrast, to reverse the terahertz waveform from the LiNbO₃ source, we make use of 2 wire-grid polarizers at angles of, respectively, $\pm 45^\circ$ and 90° relative to the polarization of the incident terahertz beam. We note that this commonly used projection approach leads to terahertz amplitude losses of $\geq 50\%$.

To demonstrate the implications of such field reversal, we measure the electro-optic signal and terahertz-Kerr effect again for terahertz pulses from LiNbO₃ after the 2 polarizers for field reversal. The result is shown by the pink solid lines in Figs. 5(a) and 5(b): the terahertz electric field is reduced by about 50% [Fig. 5(a)], while the terahertz-Kerr-effect amplitude reduces to $< 25\%$ [Fig. 5(b)], consistent with expectations. Such signal reduction does not occur for the STE setup.

IV. CONCLUSION

Our results demonstrate a significant performance improvement of STEs, which is a direct consequence of the improved thermal and photonic configuration. For high-energy and large-area operation, the Si-STE design exhibits a 4-fold and even 36-fold enhancement in terms of terahertz power compared to a standard STE on sapphire and glass, respectively [17]. The broadband terahertz fields from this easy-to-use source are highly interesting for spectroscopic studies of the linear and nonlinear response

of fundamental modes of all phases of matter over a broad range of frequencies and pump fluences.

ACKNOWLEDGMENTS

The authors thank Oliver Gueckstock for fruitful discussions and Amon Ruge and Afnan Alostaz for help with measurements. The authors acknowledge funding by the DFG collaborative research center SFB TRR 227 “Ultrafast spin dynamics” (project ID 328545488, projects A05, B02, and B05), the DFG priority program SPP2314 INTEREST (project ITISA), the ERC H2020 CoG project TERAMAG/Grant No. 681917, the DFG collaborative research center SFB TRR 173 “Spin + X” (project ID 268565370, projects A01, B02), ERC-2019-SyG 3D MAGiC/Grant No. 856538 and MSCA ITN MagnEfi/Grant No. 860060. The authors acknowledge financial support from the Horizon 2020 Framework Programme of the European Commission under FET Open Grant No. 863155 (s-Nebula). R.R. also acknowledges support by the International Max Planck Research School (IMPRS) for Elementary Processes in Physical Chemistry.

T.S.S. and T.K. are shareholders of TeraSpinTec GmbH, and T.S.S. is an employee of TeraSpinTec GmbH.

-
- [1] S. L. Dexheimer, *Terahertz spectroscopy: principles and applications* (CRC Press, Boca Raton, 2017).
- [2] W. Zhang, P. Maldonado, Z. Jin, T. S. Seifert, J. Arabshi, G. Schmerber, E. Beaupaire, M. Bonn, T. Kampfrath, P. M. Oppeneer, *et al.*, Ultrafast terahertz magnetometry, *Nat. Commun.* **11**, 4247 (2020).
- [3] H.-J. Song and T. Nagatsuma, *Handbook of terahertz technologies: devices and applications* (Jenny Stanford Publishing, New York, 2015).
- [4] T. Kampfrath, K. Tanaka, and K. A. Nelson, Resonant and nonresonant control over matter and light by intense terahertz transients, *Nat. Photonics* **7**, 680 (2013).
- [5] H. Y. Hwang, S. Fleischer, N. C. Brandt, B. G. Perkins Jr, M. Liu, K. Fan, A. Sternbach, X. Zhang, R. D. Averitt, and K. A. Nelson, A review of non-linear terahertz spectroscopy with ultrashort tabletop-laser pulses, *J. Mod. Opt.* **62**, 1447 (2015).
- [6] D. Nicoletti and A. Cavalleri, Nonlinear light–matter interaction at terahertz frequencies, *Adv. Opt. Photonics* **8**, 401 (2016).
- [7] M. C. Hoffmann and J. A. Fülöp, Intense ultrashort terahertz pulses: Generation and applications, *J. Phys. D* **44**, 17 (2011).
- [8] E. Isgandarov, X. Ropagnol, M. Singh, and T. Ozaki, Intense terahertz generation from photoconductive antennas, *Front. Optoelectron.* **14**, 64 (2021).
- [9] A. Singh, A. Pashkin, S. Winnerl, M. Helm, and H. Schneider, Gapless broadband terahertz emission from a germanium photoconductive emitter, *ACS Photonics* **5**, 2718 (2018).
- [10] C. W. Berry, N. Wang, M. R. Hashemi, M. Unlu, and M. Jarrahi, Significant performance enhancement in photoconductive terahertz optoelectronics by incorporating plasmonic contact electrodes, *Nat. Commun.* **4**, 1622 (2013).
- [11] C. Meineke, M. Prager, J. Hayes, Q. Wen, L. Z. Kastner, D. Schuh, K. Fritsch, O. Pronin, M. Stein, F. Schäfer, *et al.*, Scalable high-repetition-rate sub-half-cycle terahertz pulses from spatially indirect interband transitions, *Light Sci. Appl.* **11**, 151 (2022).
- [12] V. Y. Fedorov and S. Tzortzakis, Extreme THz fields from two-color filamentation of midinfrared laser pulses, *Phys. Rev. A* **97**, 063842 (2018).
- [13] E. Matsubara, M. Nagai, and M. Ashida, Ultrabroadband coherent electric field from far infrared to 200 THz using air plasma induced by 10 fs pulses, *Appl. Phys. Lett.* **101**, 011105 (2012).
- [14] T. Bartel, P. Gaal, K. Reimann, M. Woerner, and T. Elsaesser, Generation of single-cycle THz transients with high electric-field amplitudes, *Opt. Lett.* **30**, 2805 (2005).
- [15] S. Liu, C. Lu, Z. Fan, S. Wang, P. Li, X. Chen, J. Pan, Y. Xu, Y. Liu, and X. Wu, Modulated terahertz generation in femtosecond laser plasma filaments by high-field spintronic terahertz pulses, *Appl. Phys. Lett.* **120**, 172404 (2022).
- [16] T. Seifert, S. Jaiswal, U. Martens, J. Hannegan, L. Braun, P. Maldonado, F. Freimuth, A. Kronenberg, J. Henrizi, I. Radu, *et al.*, Efficient metallic spintronic emitters of ultrabroadband terahertz radiation, *Nat. Photonics* **10**, 483 (2016).
- [17] T. Seifert, S. Jaiswal, M. Sajadi, G. Jakob, S. Winnerl, M. Wolf, M. Kläui, and T. Kampfrath, Ultrabroadband single-cycle terahertz pulses with peak fields of 300 kV cm^{-1} from a metallic spintronic emitter, *Appl. Phys. Lett.* **110**, 252402 (2017).
- [18] T. Vogel, A. Omar, S. Mansourzadeh, F. Wulf, N. M. Sabanés, M. Müller, T. S. Seifert, A. Weigel, G. Jakob, M. Kläui, *et al.*, Average power scaling of THz spintronic emitters efficiently cooled in reflection geometry, *Opt. Express* **30**, 20451 (2022).
- [19] J. A. Fülöp, S. Tzortzakis, and T. Kampfrath, Laser-driven strong-field terahertz sources, *Adv. Opt. Mater.* **8**, 1900681 (2020).
- [20] C. Bull, S. M. Hewett, R. Ji, C.-H. Lin, T. Thomson, D. M. Graham, and P. W. Nutter, Spintronic terahertz emitters: Status and prospects from a materials perspective, *APL Mater.* **9**, 090701 (2021).
- [21] T. S. Seifert, L. Cheng, Z. Wei, T. Kampfrath, and J. Qi, Spintronic sources of ultrashort terahertz electromagnetic pulses, *Appl. Phys. Lett.* **120**, 180401 (2022).
- [22] H. Hirori, A. Doi, F. Blanchard, and K. Tanaka, Single-cycle terahertz pulses with amplitudes exceeding 1 MV/cm generated by optical rectification in LiNbO_3 , *Appl. Phys. Lett.* **98**, 091106 (2011).
- [23] S. S. Dhillon, M. S. Vitiello, E. H. Linfield, A. G. Davies, M. C. Hoffmann, J. Booske, C. Paoloni, M. Gensch, P. Weightman, G. P. Williams, *et al.*, The 2017 terahertz science and technology roadmap, *J. Phys. D: Appl. Phys.* **50**, 043001 (2017).
- [24] C. Rader, Z. B. Zaccardi, S.-H. E. Ho, K. G. Harrell, P. K. Petersen, M. F. Nielson, H. Stephan, N. K. Green, D. J. H. Ludlow, M. J. Lutz, *et al.*, A new standard in high-field

- terahertz generation: The organic nonlinear optical crystal PNPA, *ACS Photonics* **9**, 3720 (2022).
- [25] H. Zhao, Y. Tan, T. Wu, G. Steinfeld, Y. Zhang, C. Zhang, L. Zhang, and M. Shalaby, Efficient broadband terahertz generation from organic crystal BNA using near infrared pump, *Appl. Phys. Lett.* **114**, 241101 (2019).
- [26] A. G. Stepanov, C. Ruchert, J. Levallois, C. Erny, and C. P. Hauri, Generation of broadband THz pulses in organic crystal OH1 at room temperature and 10 K, *Opt. Mater. Express* **4**, 870 (2014).
- [27] Y. Zhang, X. Zhang, S. Li, J. Gu, Y. Li, Z. Tian, C. Ouyang, M. He, J. Han, and W. Zhang, A broadband THz-TDS system based on DSTMS emitter and LTG InGaAs/InAlAs photoconductive antenna detector, *Sci. Rep.* **6**, 26949 (2016).
- [28] F. Roeder, M. Shalaby, B. Beleites, F. Ronneberger, and A. Gopal, THz generation by optical rectification of intense near-infrared pulses in organic crystal BNA, *Opt. Express* **28**, 36274 (2020).
- [29] M. D. Thomson, V. Blank, and H. G. Roskos, Terahertz white-light pulses from an air plasma photo-induced by incommensurate two-color optical fields, *Opt. Express* **18**, 23173 (2010).
- [30] K. L. Yeh, M. C. Hoffmann, J. Hebling, and K. A. Nelson, Generation of 10 μ J ultrashort terahertz pulses by optical rectification, *Appl. Phys. Lett.* **90**, 171121 (2007).
- [31] J. Hebling, G. Almasi, I. Kozma, and J. Kuhl, Velocity matching by pulse front tilting for large area THz-pulse generation, *Opt. Express* **10**, 1161 (2002).
- [32] B. Zhang, Z. Ma, J. Ma, X. Wu, C. Ouyang, D. Kong, T. Hong, X. Wang, P. Yang, L. Chen, *et al.*, 1.4-mJ high energy terahertz radiation from lithium niobates, *Laser Photonics Rev.* **15**, 2000295 (2021).
- [33] D. Yang, J. Liang, C. Zhou, L. Sun, R. Zheng, S. Luo, Y. Wu, and J. Qi, Powerful and tunable THz emitters based on the Fe/Pt magnetic heterostructure, *Adv. Opt. Mater.* **4**, 1944 (2016).
- [34] Y. Wu, M. Elyasi, X. Qiu, M. Chen, Y. Liu, L. Ke, and H. Yang, High-performance THz emitters based on ferromagnetic/nonmagnetic heterostructures, *Adv. Mater.* **29**, 1603031 (2017).
- [35] G. Torosyan, S. Keller, L. Scheuer, R. Beigang, and E. T. Papaioannou, Optimized spintronic terahertz emitters based on epitaxial grown Fe/Pt layer structures, *Sci. Rep.* **8**, 1311 (2018).
- [36] E. T. Papaioannou and R. Beigang, THz spintronic emitters: A review on achievements and future challenges, *Nanophotonics* **10**, 1243 (2021).
- [37] T. J. Huisman, R. V. Mikhaylovskiy, J. D. Costa, F. Freimuth, E. Paz, J. Ventura, P. P. Freitas, S. Blügel, Y. Mokrousov, T. Rasing, *et al.*, Femtosecond control of electric currents in metallic ferromagnetic heterostructures, *Nat. Nanotechnol.* **11**, 455 (2016).
- [38] G. Li, R. Medapalli, R. V. Mikhaylovskiy, F. E. Spada, T. Rasing, E. E. Fullerton, and A. V. Kimel, THz emission from Co/Pt bilayers with varied roughness, crystal structure, and interface intermixing, *Phys. Rev. Mater.* **3**, 084415 (2019).
- [39] R. Schneider, M. Fix, J. Bensmann, S. M. d. Vasconcellos, M. Albrecht, and R. Bratschitsch, Spintronic GdFe/Pt THz emitters, *Appl. Phys. Lett.* **115**, 152401 (2019).
- [40] M. Fix, R. Schneider, J. Bensmann, S. M. d. Vasconcellos, R. Bratschitsch, and M. Albrecht, Thermomagnetic control of spintronic THz emission enabled by ferrimagnets, *Appl. Phys. Lett.* **116**, 012402 (2020).
- [41] J. Hawecker, T.-H. Dang, E. Rongione, J. Boust, S. Collin, J.-M. George, H.-J. Drouhin, Y. Laplace, R. Grasset, J. Dong, *et al.*, Spin injection efficiency at metallic interfaces probed by THz emission spectroscopy, *Adv. Opt. Mater.* **9**, 2100412 (2021).
- [42] W. Wu, C. Y. Ameyaw, M. F. Doty, and M. B. Jungfleisch, Principles of spintronic THz emitters, *J. Appl. Phys.* **130**, 091101 (2021).
- [43] W. Wu, S. Lendinez, M. T. Kaffash, R. D. Schaller, H. Wen, and M. B. Jungfleisch, Modification of terahertz emission spectrum using microfabricated spintronic emitters, *J. Appl. Phys.* **128**, 103902 (2020).
- [44] M. Chen, Y. Wu, Y. Liu, K. Lee, X. Qiu, P. He, J. Yu, and H. Yang, Current-enhanced broadband THz emission from spintronic devices, *Adv. Opt. Mater.* **7**, 1801608 (2018).
- [45] F.-F. Stiewe, T. Winkel, Y. Sasaki, T. Tubandt, T. Kleinke, C. Denker, U. Martens, N. Meyer, T. S. Parvini, S. Mizukami, *et al.*, Spintronic emitters for super-resolution in THz-spectral imaging, *Appl. Phys. Lett.* **120**, 032406 (2022).
- [46] Y. Ogasawara, Y. Sasaki, S. Iihama, A. Kamimaki, K. Z. Suzuki, and S. Mizukami, Laser-induced terahertz emission from layered synthetic magnets, *Appl. Phys. Express* **13**, 063001 (2020).
- [47] R. Adam, G. Chen, D. E. Bürgler, T. Shou, I. Komissarov, S. Heidtfeld, H. Hardtdegen, M. Mikulics, C. M. Schneider, and R. Sobolewski, Magnetically and optically tunable terahertz radiation from Ta/NiFe/Pt spintronic nanolayers generated by femtosecond laser pulses, *Appl. Phys. Lett.* **114**, 212405 (2019).
- [48] N. Awari, S. Kovalev, C. Fowley, K. Rode, R. A. Gallardo, Y.-C. Lau, D. Betto, N. Thiagarajah, B. Green, O. Yildirim, *et al.*, Narrow-band tunable terahertz emission from ferrimagnetic $Mn_{3-x}Ga$ thin films, *Appl. Phys. Lett.* **109**, 032403 (2016).
- [49] M. T. Hibberd, D. S. Lake, N. A. B. Johansson, T. Thomson, S. P. Jamison, and D. M. Graham, Magnetic-field tailoring of the terahertz polarization emitted from a spintronic source, *Appl. Phys. Lett.* **114**, 031101 (2019).
- [50] D. Kong, X. Wu, B. Wang, T. Nie, M. Xiao, C. Pandey, Y. Gao, L. Wen, W. Zhao, C. Ruan, *et al.*, Broadband spintronic terahertz emitter with magnetic-field manipulated polarizations, *Adv. Opt. Mater.* **7**, 1900487 (2019).
- [51] H. Niwa, N. Yoshikawa, M. Kawaguchi, M. Hayashi, and R. Shimano, Switchable generation of azimuthally- and radially-polarized terahertz beams from a spintronic terahertz emitter, *Opt. Express* **29**, 13331 (2021).
- [52] X. Chen, X. Wu, S. Shan, F. Guo, D. Kong, C. Wang, T. Nie, C. Pandey, L. Wen, W. Zhao, *et al.*, Generation and manipulation of chiral broadband terahertz waves from cascade spintronic terahertz emitters, *Appl. Phys. Lett.* **115**, 221104 (2019).

- [53] R. Rouzegar, L. Brandt, L. Nádvorník, D. A. Reiss, A. L. Chekhov, O. Gueckstock, C. In, M. Wolf, T. S. Seifert, P. W. Brouwer, *et al.*, Laser-induced terahertz spin transport in magnetic nanostructures arises from the same force as ultrafast demagnetization, *Phys. Rev. B* **106**, 144427 (2022).
- [54] P. Jiménez-Cavero, O. Gueckstock, L. Nádvorník, I. Lucas, T. S. Seifert, M. Wolf, R. Rouzegar, P. W. Brouwer, S. Becker, G. Jakob, *et al.*, Transition of laser-induced terahertz spin currents from torque- to conduction-electron-mediated transport, *Phys. Rev. B* **105**, 184408 (2022).
- [55] G. Bierhance, A. Markou, O. Gueckstock, R. Rouzegar, Y. Behovits, A. L. Chekhov, M. Wolf, T. S. Seifert, C. Felser, and T. Kampfrath, Spin-voltage-driven efficient terahertz spin currents from the magnetic Weyl semimetals Co_2MnGa and Co_2MnAl , *Appl. Phys. Lett.* **120**, 082401 (2022).
- [56] O. Gueckstock, L. Nádvorník, M. Gradhand, T. S. Seifert, G. Bierhance, R. Rouzegar, M. Wolf, M. Vafaee, J. Cramer, M. A. Syskaki, *et al.*, Terahertz spin-to-charge conversion by interfacial skew scattering in metallic bilayers, *Adv. Mater.* **33**, 2006281 (2021).
- [57] T. S. Seifert, N. M. Tran, O. Gueckstock, S. M. Rouzegar, L. Nadvornik, S. Jaiswal, G. Jakob, V. V. Temnov, M. Münzenberg, M. Wolf, *et al.*, Terahertz spectroscopy for all-optical spintronic characterization of the spin-Hall-effect metals Pt, W and $\text{Cu}_{80}\text{Ir}_{20}$, *J. Phys. D: Appl. Phys.* **51**, 364003 (2018).
- [58] H. S. Qiu, K. Kato, K. Hirota, N. Sarukura, M. Yoshimura, and M. Nakajima, Layer thickness dependence of the terahertz emission based on spin current in ferromagnetic heterostructures, *Opt. Express* **26**, 15247 (2018).
- [59] O. Gueckstock, L. Nádvorník, T. S. Seifert, M. Borchert, G. Jakob, G. Schmidt, G. Woltersdorf, M. Kläui, M. Wolf, and T. Kampfrath, Modulating the polarization of broadband terahertz pulses from a spintronic emitter at rates up to 10 kHz, *Optica* **8**, 1013 (2021).
- [60] Z. Feng, H. Qiu, D. Wang, C. Zhang, S. Sun, B. Jin, and W. Tan, Spintronic terahertz emitter, *J. Appl. Phys.* **129**, 010901 (2021).
- [61] M. A. Wahada, E. Şaşıoğlu, W. Hoppe, X. Zhou, H. Deniz, R. Rouzegar, T. Kampfrath, I. Mertig, S. S. P. Parkin, and G. Woltersdorf, Atomic scale control of spin current transmission at interfaces, *Nano Lett.* **22**, 3539 (2022).
- [62] U. Nandi, M. S. Abdelaziz, S. Jaiswal, G. Jakob, O. Gueckstock, S. M. Rouzegar, T. S. Seifert, M. Kläui, T. Kampfrath, and S. Preu, Antenna-coupled spintronic terahertz emitters driven by a 1550 nm femtosecond laser oscillator, *Appl. Phys. Lett.* **115**, 022405 (2019).
- [63] R. I. Herapath, S. M. Hornett, T. S. Seifert, G. Jakob, M. Kläui, J. Bertolotti, T. Kampfrath, and E. Hendry, Impact of pump wavelength on terahertz emission of a cavity-enhanced spintronic trilayer, *Appl. Phys. Lett.* **114**, 041107 (2019).
- [64] P. Koleják, G. Lezier, L. Halagačka, Z. Gelnárová, J.-F. Lampin, N. Tiercelin, M. Vanwolleghem, and K. Postava, in *2022 47th International Conference on Infrared, Millimeter and Terahertz Waves (IRMMW-THz)* (IEEE, 2022), p. 1.
- [65] N. C. Passler, M. Jeannin, and A. Paarmann, Layer-resolved absorption of light in arbitrarily anisotropic heterostructures, *Phys. Rev. B* **101**, 165425 (2020).
- [66] H. Jang, J. Kimling, and D. G. Cahill, Nonequilibrium heat transport in Pt and Ru probed by an ultrathin Co thermometer, *Phys. Rev. B* **101**, 064304 (2020).
- [67] H. R. Shanks, P. D. Maycock, P. H. Sidles, and G. C. Danielson, Thermal Conductivity of Silicon from 300 to 1400°K, *Phys. Rev.* **130**, 1743 (1963).
- [68] D. T. Morelli, C. P. Beetz, and T. A. Perry, Thermal conductivity of synthetic diamond films, *J. Appl. Phys.* **64**, 3063 (1988).
- [69] M. J. Assael, K. D. Antoniadis, and J. Wu, New measurements of the thermal conductivity of PMMA, BK7, and Pyrex 7740 up to 450 K, *Int. J. Thermophys.* **29**, 1257 (2008).
- [70] See Supplemental Material at <http://link.aps.org/supplemental/10.1103/PhysRevApplied.19.034018> for more figures and details.
- [71] L. Nádvorník, M. Borchert, L. Brandt, R. Schlitz, K. A. de Mare, K. Výborný, I. Mertig, G. Jakob, M. Kläui, S. T. B. Goennenwein, *et al.*, Broadband Terahertz Probes of Anisotropic Magnetoresistance Disentangle Extrinsic and Intrinsic Contributions, *Phys. Rev. X* **11**, 021030 (2021).
- [72] A. Leitenstorfer, S. Hunsche, J. Shah, M. C. Nuss, and W. H. Knox, Detectors and sources for ultrabroadband electro-optic sampling: Experiment and theory, *Appl. Phys. Lett.* **74**, 1516 (1999).
- [73] T. Kampfrath, J. Nötzold, and M. Wolf, Sampling of broadband terahertz pulses with thick electro-optic crystals, *Appl. Phys. Lett.* **90**, 231113 (2007).
- [74] N. C. J. van der Valk, T. Wenckeback, and P. C. M. Planken, Full mathematical description of electro-optic detection in optically isotropic crystals, *J. Opt. Soc. Am. B* **21**, 622 (2004).
- [75] A. L. Chekhov, Y. Behovits, J. J. F. Heitz, C. Denker, D. A. Reiss, M. Wolf, M. Weinelt, P. W. Brouwer, M. Münzenberg, and T. Kampfrath, Ultrafast Demagnetization of Iron Induced by Optical versus Terahertz Pulses, *Phys. Rev. X* **11**, 041055 (2021).
- [76] S. F. Maehrlein, I. Radu, P. Maldonado, A. Paarmann, M. Gensch, A. M. Kalashnikova, R. V. Pisarev, M. Wolf, P. M. Oppeneer, J. Barker, *et al.*, Dissecting spin-phonon equilibration in ferrimagnetic insulators by ultrafast lattice excitation, *Sci. Adv.* **4**, eaar5164 (2018).
- [77] M. Sajadi, M. Wolf, and T. Kampfrath, Terahertz-field-induced optical birefringence in common window and substrate materials, *Opt. Express* **23**, 28985 (2015).
- [78] I. P. Kaminow and E. H. Turner, *Handbook of Lasers* (Chemical Rubber Co., Cleveland, OH, 1971), pp. 447.
- [79] J. Worlock, in *Laser Handbook*, edited by F. T. Arecchi, E. O. Schulz-Dubois (North-Holland, Amsterdam, 1972).
- [80] Y. Berozashvili, S. Machavariani, A. Natsvlishvili, and A. Chirakadze, Dispersion of the linear electro-optic coefficients and the non-linear susceptibility in GaP, *J. Phys. D: Appl. Phys.* **22**, 682 (1989).
- [81] L. Guiramand, J. E. Nkeck, X. Ropagnol, T. Ozaki, and F. Blanchard, Near-optimal intense and powerful terahertz source by optical rectification in lithium niobate crystal, *Photonics Res.* **10**, 340 (2022).

- [82] M. Cornet, J. Degert, E. Abraham, and E. Freysz, Terahertz Kerr effect in gallium phosphide crystal, *J. Opt. Soc. Am. B* **31**, 1648 (2014).
- [83] M. F. Nielson, S.-H. Ho, C. D. Moss, J. Dominguez, and J. A. Johnson, in *Frontiers in Optics + Laser Science 2022 (FIO, LS)* (Optica Publishing Group, 2022), p. JTU4B.19.
- [84] M. Hudl, M. d'Aquino, M. Pancaldi, S.-H. Yang, M. G. Samant, S. S. P. Parkin, H. A. Dürr, C. Serpico, M. C. Hoffmann, and S. Bonetti, Nonlinear Magnetization Dynamics Driven by Strong Terahertz Fields, *Phys. Rev. Lett.* **123**, 197204 (2019).
- [85] T. L. Cocker, D. Peller, P. Yu, J. Repp, and R. Huber, Tracking the ultrafast motion of a single molecule by femtosecond orbital imaging, *Nature* **539**, 263 (2016).
- [86] M. Abdo, S. Sheng, S. Rolf-Pissarczyk, L. Arnhold, J. A. J. Burgess, M. Isobe, L. Malavolti, and S. Loth, Variable repetition rate THz source for ultrafast scanning tunneling microscopy, *ACS Photonics* **8**, 702 (2021).